

EFFICIENT MULTI-OBJECTIVE DESIGN OPTIMIZATION OF ROTOR AIRFOILS FOR IMPROVING DYNAMIC STALL CHARACTERISTICS

Zuo Lu^{1,2}, Zhong-Hua Han^{1,2}, Wen-Ping Song^{1,2}, Ke-Shi Zhang^{1,2} &Kang-Yuan Zhou^{1,2}

School of Aeronautics, Northwestern Polytechnical University, Xi'an 710072, China.
 National Key Laboratory of Aircraft Configuration Design, Xi'an 710072, China.

Abstract

The dynamic stall characteristics of an airfoil limit the aerodynamic performance of a rotor. To improve the dynamic stall characteristics of the rotor airfoil, an efficient multi-objective aerodynamic shape design optimization method for rotor airfoils based on Computational Fluid Dynamics and numerical optimization algorithms is developed. This method employs the efficient surrogate-based multi-objective optimization (SBMO) algorithm, which enhances optimization efficiency and convergence through decomposition and cooperation. The perturbed CST method was used for airfoil parameterization. By applying the developed method, the optimized airfoil showed significant improvement in dynamic stall characteristics, with the peak pitching moment coefficient reduced by 38.8%. Additionally, a multi-objective optimization design considering both dynamic stall characteristics and static aerodynamic characteristics in hovering was conducted, resulting in a Pareto front with 33 solutions. The optimal airfoils selected from this Pareto front focus on different aerodynamic characteristics. One selected airfoil effectively balances both aspects, reducing the peak pitching moment coefficient by 19.71% and the static drag coefficient in hovering by 10.70%.

Keywords: dynamic stall, rotor airfoil design, multi-objective optimization, surrogate-based algorithm

1. Introduction

Helicopter rotor airfoils operate in highly unsteady conditions, primarily due to the complex motions of pitching, flapping, and rotation. The dynamic stall phenomenon commonly occurs on the retreating side of the rotor during forward flight. This phenomenon causes a sudden decrease in rotor airfoil lift and a surge in pitching moment, which can result in stall flutter. Dynamic stall significantly impacts the rotor's aerodynamic performance, restricting the helicopter's operational capabilities and limiting its forward flight speed. [1][2] Therefore, controlling the dynamic stall characteristics of rotor airfoils is crucial for enhancing helicopter performance.

In recent years, to improve the dynamic stall characteristics of rotor airfoils, more and more research has utilized aerodynamic design optimization methods to optimize the aerodynamic shape of rotor airfoils. This method, based on Computational Fluid Dynamics (CFD) and numerical optimization algorithms, can eliminate the reliance on designer experience and effectively search for optimal solutions within the design space. Mani [3] employed the adjoint method to optimize the dynamic stall characteristics of a SC1095 airfoils, weakening the generation and development of dynamic separation vortices. Wang [4] used sequential quadratic programming (SQP) method to optimize the dynamic stall characteristics of an OA209 airfoil and validated the aerodynamic performance of the optimized airfoil on three-dimensional rotor blades.

To further improve optimization efficiency, some studies have started using surrogate models to replace expensive CFD calculations, significantly reducing computation time. Liu [5] used deep neural network (DNN) to replace time-consuming high-fidelity unsteady numerical simulations of rotor airfoils. The time of optimization was reduced by an order of magnitude. Raul [6][7] used kriging and co-kriging models, along with infill-sampling criteria, to achieve efficient optimization of the dynamic stall characteristics of the NACA0012 airfoil, balancing optimization efficiency and global search capability. These studies show that surrogate-based optimization methods can effectively improve the efficiency of the optimization of dynamic stall characteristics of rotor airfoils, making

them a highly promising aerodynamic shape optimization approach which is also indicted in steady optimizations [8][9].

Additionally, most of the mentioned studies only considered the dynamic stall characteristics of rotor airfoils. For rotor airfoils, their static aerodynamic characteristics, such as drag characteristics at hovering condition, are equally important. Whether airfoils optimized for dynamic characteristics can maintain good static aerodynamic characteristics remains to be studied. Wang [10] calculated the static aerodynamic characteristics, such as lift, drag, and pitching moment coefficient of airfoils optimized for dynamic stall characteristics, at the same Mach number. The results showed that the optimized airfoil also had better potential static aerodynamic performance than the baseline airfoil. However, this study was retrospective and did not consider static aerodynamic characteristics during the optimization.

Motivated by that, this paper implements an efficient surrogate-based rotor airfoil aerodynamic design optimization method. By employing this method, rotor airfoils have been optimized to improve dynamic stall characteristics. Additionally, a multi-objective optimization considering both dynamic stall and static aerodynamic characteristics has been performed, exploring the conflicting relationship between these characteristics.

2. Methodology

2.1 Airfoil Parametrization Method

This paper adopts a variant of the CST method, called the perturbed CST method, to parameterize the airfoil. This method uses the original CST equation [11] as a perturbation of the baseline airfoil's geometric coordinates, adding it to the baseline airfoil's geometric coordinates to obtain a new airfoil. The general expression of the perturbed CST parameterization method is as follows:

$$y(x) = y_0(x) + x^{N_1} \bullet (1 - x)^{N_2} \bullet \sum_{i=0}^{N} A_i \bullet x^i$$
 (1)

Here, $y_0(x)$ represents the vertical coordinate of the baseline airfoil. C(x) and S(x) denote the shape and class function in the original CST method, respectively, and are defined as follows:

$$C(x) = x^{N_1} \bullet (1-x)^{N_2}$$

$$S(x) = \sum_{i=0}^{N} A_i \cdot \frac{N!}{i!(N-i)!} x^i (1-x)^{N-i}$$
(2)

In the class function C(x), the parameters N_1 and N_2 are typically set to 0.5 and 1.0, respectively, for a general blunt leading edge and sharp trailing edge airfoil. The shape function S(x) is a Bernstein polynomial, where N represents the order, and A_i is the parameter to be determined, serving as the control parameter of the perturbed CST parameterization method.

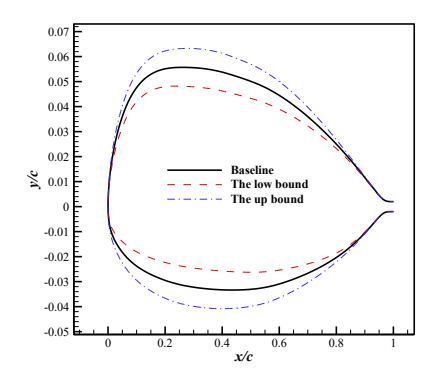


Figure 1 – The design space defined by the perturbed CST method

The advantage of this method is that in the aerodynamic optimization of rotor airfoils, there is no need to perturb the baseline airfoil's CST parameters to define the design space. Instead, the range of design variables (the perturbed CST parameters) can be directly specified. For example, the design space defined by $\mathbf{x} \in \prod_{j=1}^{18} [-0.02, 0.02]$ (the 8th-order perturbed CST) is shown in Figure 1.

2.2 The Surrogate-Based Multi-Objective Optimization Algorithm

This paper adopts the Surrogate-Based Multi-Objective (SBMO) optimization algorithm [12][13] for rotor airfoil optimization which is coded in our own optimizer, SurroOpt [14]. The framework of the SBMO algorithm is shown in Figure 2, and its main steps are as follows:

- **Step 1: Design of Experiments (DoE).** First, use a design of experiments method, such as Latin Hypercube Sampling (LHS), to select several initial sample points from the design space. Use a CFD solver to obtain the objective and constraint function response values for these initial sample points, forming the initial sample set.
- **Step 2: Build surrogate models.** Based on the initial sample set obtained in the previous step, build surrogate models for each objective and constraint function.
- **Step 3: Decompose the multi-objective problem.** Decompose the multi-objective problem into several single-objective optimization sub-problems by adopting the Tchebycheff decomposition approaching.
- **Step 4: Select new sample points.** Use a combination strategy of infill-sampling criteria to construct a series of corresponding acquisition problems, solving them to obtain a series of new sample points in one optimization.
- **Step 5: Update surrogate models.** Evaluate the new sample points obtained in the previous step and use them to update the surrogate models. Repeat steps (2) to (4) until the convergence criteria are met.

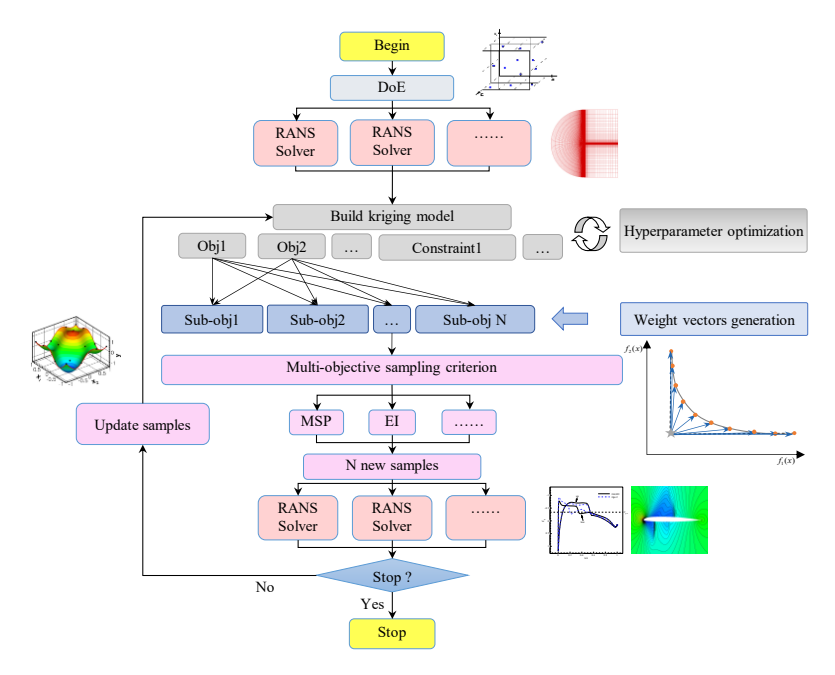


Figure 2 – Framework of the SBMO algorithm

2.2.1 Kriging Model

In this paper, we employ the kriging model [15][16] due to its strong ability to predict multidimensional and highly nonlinear response surfaces. It also has a unique capability to indicate prediction uncertainty by providing an error estimation, which can be used to guide the sampling of new points.

The predictor of a unknown function y = f(x) and the mean squared error (MSE) given by kriging model are formula as follow:

$$\hat{y}(\mathbf{x}) = \hat{\beta}_0 + \mathbf{r}^T \mathbf{R}^{-1} \left(\mathbf{y}_S - \hat{\beta}_0 \mathbf{F} \right)$$

$$MSE[\hat{y}(\mathbf{x})] = s^2(\mathbf{x}) = \sigma^2 \left(1 - \mathbf{r}^T \mathbf{R}^{-1} \mathbf{r} + \frac{\left(1 - \mathbf{F}^T \mathbf{R}^{-1} \mathbf{r} \right)^2}{\mathbf{F}^T \mathbf{R}^{-1} \mathbf{F}} \right)$$
(3)

where, $\hat{y}(\mathbf{x})$ and $\mathbf{y}_s = (y_1, \dots, y_N)^T$ denote the predictor and the observed responses, respectively. $\mathbf{F} = [1, \dots, 1]^T \in \mathbb{R}^N$ is a unit column vector., the correlation matrix \mathbf{R} and correlation vector \mathbf{r} is defined as follows:

$$\mathbf{R} := \left[R\left(\mathbf{x}^{(i)}, \mathbf{x}^{(j)}\right) \right]_{ij} \in \mathbb{R}^{N \times N}$$

$$\mathbf{r} := \left[R\left(\mathbf{x}^{(i)}, \mathbf{x}\right) \right]_{i} \in \mathbb{R}^{N}$$
(4)

here R is the spatial correlation function that only depends on the Euclidean distance between two $\mathbf{x}^{(i)}$ and $\mathbf{x}^{(j)}$. The β_0 and σ^2 is defined as follows:

$$\beta_0 = (\mathbf{F}^T \mathbf{R}^{-1} \mathbf{F})^{-1} \mathbf{F}^T \mathbf{R}^{-1} \mathbf{y}_S$$

$$\sigma^2 = \frac{1}{n} (\mathbf{y}_S - \beta_0 \mathbf{F})^T \mathbf{R}^{-1} (\mathbf{y}_S - \beta_0 \mathbf{F})$$
(5)

2.2.2 Decomposition Approaching

As for a generally continuous multi-objective problem with m objectives and n_g constraints, a single-objective optimization sub-problem decomposed by the Tchebycheff approach can be formulated as:

$$\min_{\mathbf{x} \in \Omega} g^{tc} \left(\mathbf{x} | \lambda, \mathbf{z}^* \right) = \min_{\mathbf{x} \in \Omega} \max_{1 \le i \le m} \left\{ \lambda_i \left| f_i(\mathbf{x}) - z_i^* \right| \right\}$$
 (6)

where $\lambda = (\lambda_1, \dots, \lambda_m)$ is weight vector of the sub-problem. $\mathbf{z}^* = (z_1, \dots, z_m)$ is the reference point in the objective space and in this paper, it is obtained by minimizing the kriging prediction of objectives, i.e., $z_i^* = \min \left\{ \hat{f}_i(\mathbf{x}) \right\}$.

2.2.3 Combined Infill-Sampling Criteria Strategy

In this paper, we have incorporated a combined infill-sampling criteria strategy within the SBMO algorithm. This strategy employs both the Expected Improvement (EI) and Minimizing Surrogate Prediction (MSP) infill-sampling criteria to introduce new samples simultaneously in each iteration, effectively improving the convergence and global search ability of the SBMO algorithm. And the acquisition problems defined by EI and MSP infill-sampling criteria in the case of a bi-objective problem (m=2),for i-th sub-problem ($\xi^i(\mathbf{x})$) are defined as follows.

MSP infill-sampling criteria

min.
$$\xi^{i}(\mathbf{x}) = \max \left\{ \lambda_{1}^{i} \left(\hat{f}_{1}(\mathbf{x}) - z_{1}^{*} \right), \lambda_{2}^{i} \left(\hat{f}_{2}(\mathbf{x}) - z_{2}^{*} \right) \right\}$$

$$s.t. \quad \hat{G}(\mathbf{x}) = \left(\hat{g}_{1}(\mathbf{x}), \dots, \hat{g}_{n_{g}}(\mathbf{x}) \right)^{T} \geq 0$$

$$(7)$$

where $\hat{f}(\mathbf{x})$ and $\hat{g}(\mathbf{x})$ represent the value given by kriging predictor of the objectives and constraints, respectively.

• El infill-sampling criteria [17]

min.
$$\xi^{i}(\mathbf{x}) = E^{i}[I(\mathbf{x})] \cdot \prod_{j=1}^{n_g} P[G_j \ge 0]$$
 (8)

where the EI function $E^{i}[I(\mathbf{x})]$ is defined as:

$$\begin{cases}
\left[g_{\min^{tc,i}} - \hat{g}^{tc,i}(\mathbf{x})\right] \Phi\left(\frac{g_{\min^{tc,i}} - \hat{g}^{tc,i}(\mathbf{x})}{\hat{s}^{i}(\mathbf{x})}\right) + \hat{s}^{i}(\mathbf{x}) \phi\left(\frac{g_{\min^{tc,i}} - \hat{g}^{tc,i}(\mathbf{x})}{\hat{s}^{i}(\mathbf{x})}\right), \hat{s}^{i}(\mathbf{x}) > 0 \\
0, \hat{s}^{i}(\mathbf{x}) = 0
\end{cases}$$
(9)

where Φ and ϕ represent the cumulative distribution and probability density function of a standard normal distribution, respectively. $\hat{g}^{tc,i}$ is the value of the i-th sub-problem calculated with the kriging predictor and $g_{min}^{c,i}$ is the minimum value of the sub-problem among the evaluated sample points.

And $P[G_j \ge 0]$ is the probability of satisfying the constraint at any site, which is defined as:

$$P\left[G_{j}(\mathbf{x}) \ge 0\right] = 1 - \Phi\left(-\frac{\hat{g}_{j}(\mathbf{x})}{s_{g,j}(\mathbf{x})}\right), j = 1, \dots, n_{g}$$

$$\tag{10}$$

where $s_{g,j}(\mathbf{x})$ is the standard derivation of $G_j(\mathbf{x})$, which is assumed as normally distributed.

2.3 RANS Solver Validation

In this paper, we use our own unsteady RANS solver to calculate the dynamic stall characteristics of rotor airfoils. The calculations employ an implicit dual-time method with the $k - \omega SST$ turbulence. The accuracy of the calculations is validated using the NACA0012 airfoil as a test case, with the calculation conditions being M = 0.2, Re = 1×10^6 . The motion equation of the airfoil is $\alpha = 15^\circ + 10^\circ sin(\omega t)$, with a reduced frequency k = 0.15. Each cycle consists of 144 physical time steps, with 30 subiteration steps per physical time step, and a total of 5 cycles are calculated. The convergence of force coefficient is shown in Figure 3. It can be observed that after 3 cycles, the lift, drag, and moment coefficients have formed a stable periodic solution. To ensure the convergence of the results, the evaluation of the airfoil's dynamic stall characteristics in the subsequent optimization will still use 5 computation cycles. Figure 4 compares the hysteresis loops of the lift and drag coefficients obtained from the unsteady RANS solver with the experimental values. It can be seen that the computed lift and drag coefficients match the experimental values well during the upstroke process of the airfoil. During the downstroke process, the $k-\omega$ SST turbulence model used in this paper does not accurately simulate the separation and reattachment of the vortex on the upper surface of the airfoil. This results in a slight increase in the error between the computed lift coefficient and the experimental values, but the error remains within an acceptable range. Overall, the computed results of the rotor airfoil's dynamic stall characteristics obtained by the solver used in this paper agree well with the experimental values, meeting the needs for subsequent design optimization of rotor airfoils for improving dynamic stall characteristics.

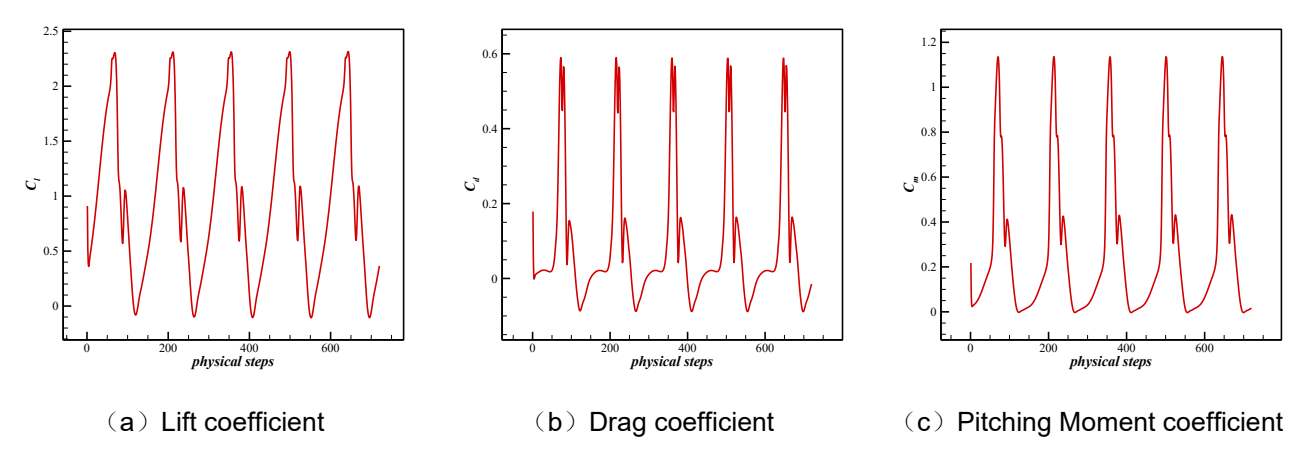


Figure 3 – Convergence curve of force coefficients in the dynamic stall characteristics calculation for the NACA0012 airfoil

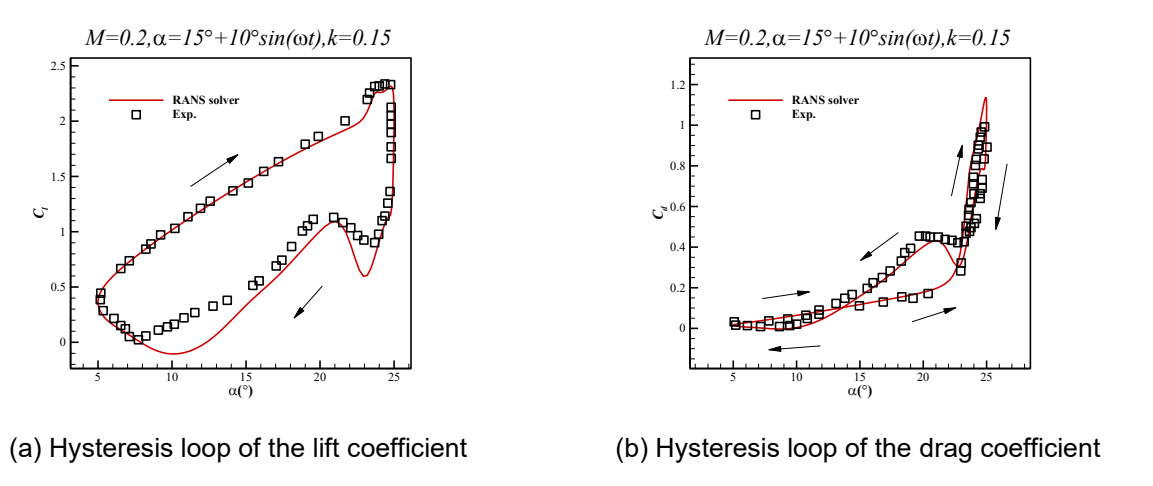


Figure 4 – The comparation of the calculated results of NACA0012 airfoil with experience data

3. Results & Discussion

3.1 Single-Objective Optimization for Improving Dynamic Stall Characteristics

Firstly, a single-objective optimization design is conducted with the goal of improving the dynamic stall characteristics of the airfoil. The design condition is Ma = 0.3, $Re = 2.03 \times 10^6$, the motion equation

of the airfoil is $\alpha = 10^{\circ} + 10^{\circ} sin(\omega t)$, and the reduced frequency is k = 0.1. The optimization objective is to reduce the peak of the pitching moment coefficient. The mathematical model for the optimization is as follows:

min.
$$\frac{\sum_{i=1}^{n_{steps}} |C_{m}^{i}|}{\sum_{i=1}^{n_{steps}} |C_{m,baseline}^{i}|}$$
s.t.
$$\sum_{i=1}^{n_{steps}} |C_{d}^{i}| < \sum_{i=1}^{n_{steps}} |C_{d,baseline}^{i}|$$

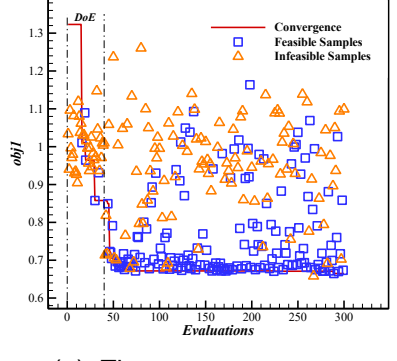
$$\sum_{i=1}^{n_{steps}} |C_{l}^{i}| > \sum_{i=1}^{n_{steps}} |C_{l,baseline}^{i}|$$

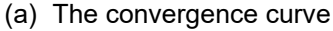
$$C_{w} > 0$$

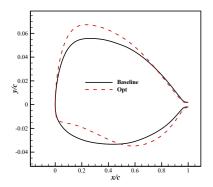
$$|t - 0.09| < 0.003$$
(11)

where, n_{steps} represents the number of physical time steps in one cycle of the unsteady calculation. C_l^i , C_d^i and C_m^i denote the instantaneous lift, drag and pitching moment coefficient of the airfoil at the i-th physical time step, respectively. $C_w = \oint C_m(\alpha) d\alpha$ represents the torsional damping factor, which must be positive to prevent an aeroelastic divergence or flutter situation promoted by dynamic stall. Symbols with the subscript "baseline" represent the aerodynamic and geometric characteristics of the baseline airfoil.

The airfoil parameterization method is an 8th-order perturbed CST, with the design space being $\mathbf{x} \in \prod_{i=1}^{18} [-0.04, 0.04]$. The initial number of sample points is 40, with a maximum of 300 sample points. The convergence curve of the optimization and geometric shape of the final optimal airfoil Opt are shown in Figure 5. Compared to the baseline airfoil, the optimal airfoil has a larger leading-edge radius and greater camber, especially in the mid-front section.







(b) The geometric shape of the optimal airfoil

Figure 5 – The convergence curve of the single-objective optimization and the optimal airfoil

The hysteresis loop of the pitching moment coefficient for the optimal airfoil is shown in Figure 6. Compared to the baseline airfoil, the peak value of the moment coefficient for the optimal airfoil has significantly decreased, with its absolute value dropping from 0.5622 to 0.3439, a reduction of 38.8%. The dynamic stall angle of attack is delayed from 19.66° to 19.91°, a delay of 0.25°. Additionally, the hysteresis loop of the pitching moment coefficient for the baseline airfoil has three loops, whereas the optimal airfoil has only two, further demonstrating the significant improvement in the dynamic stall characteristics of the optimal airfoil. The hysteresis loops of the lift and drag coefficients for the optimal airfoil are shown in Figure 7. The peak values of the lift and drag coefficients for the optimal airfoil have also been reduced, and the area of the hysteresis loop for the lift coefficient has decreased.

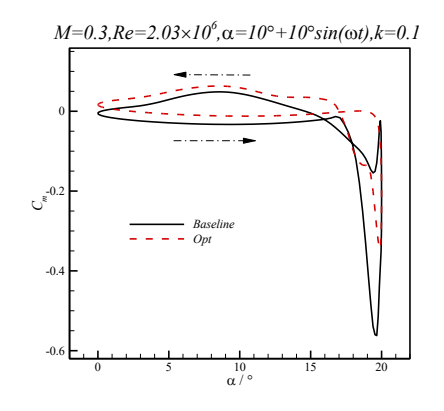
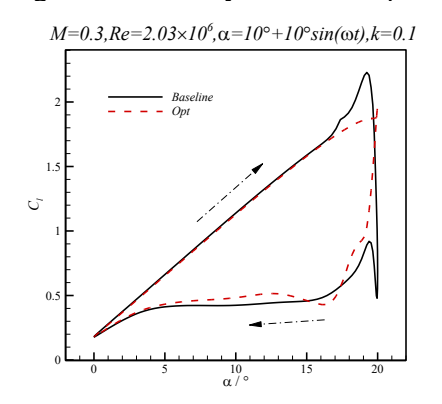
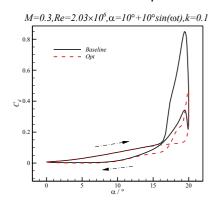


Figure 6 – The hysteresis loops of pitching moment coefficient of the optimal airfoil





- (a) Hysteresis loop of the lift coefficient
- (b) Hysteresis loop of the drag coefficient

Figure 7 – The hysteresis loops of lift and drag coefficient of the optimal airfoil

3.2 Bi-Objective Optimization for Improving Both Static and Dynamic Stall Characteristics

The single-objective design optimization significantly had been done improves the dynamic stall characteristics of the airfoil. However, the static aerodynamic characteristics of the airfoil were not considered in the optimization process. Therefore, this paper conducts a design optimization of rotor airfoils considering both dynamic stall characteristics and static aerodynamic characteristics. The optimization objective for dynamic stall characteristics is to reduce the peak of the moment coefficient. The design condition is Ma = 0.3, $Re = 2.03 \times 10^6$, the motion equation of the airfoil is $\alpha = 10^\circ + 10^\circ sin(\omega t)$, and the reduced frequency is k = 0.1. The optimization objective for static aerodynamic characteristics is to reduce the drag in hovering condition, with the design condition being Ma = 0.6, $C_l = 0.6$, $Re = 4.06 \times 10^6$. Additionally, we constrain the static maximum lift coefficient of the airfoil at Ma = 0.3, $Re = 2.03 \times 10^6$. The mathematical model for the design optimization is as follows:

min.
$$Obj1 = C_d / C_{d,baseline} |_{M=0.6, C_l=0.6}$$

min. $Obj2 = \frac{\sum_{i=1}^{n_{steps}} |C_m^i|}{\sum_{i=1}^{n_{steps}} |C_{m,baseline}^i|}$
s.t. $C_{l,max} > C_{l,max,baseline} |_{M=0.3}$
 $\sum_{i=1}^{n_{steps}} |C_l^i| > \sum_{i=1}^{n_{steps}} |C_{l,baseline}^i|$
 $C_w > 0$
 $|t-0.09| < 0.003$ (12)

where C_d represents the static drag coefficient, and $C_{l,\max}$ represents the static maximum lift coefficient. To expand the design space, the airfoil parameterization method uses a 12th-order perturbed CST, with the design space being $\mathbf{x} \in \prod_{i=1}^{26} [-0.04, 0.04]$. The initial number of sample points is 40, with a maximum of 440 sample points. In each round, 20 new selected points are added using the combined infill-sampling criteria strategy.

After 20 iterations, a Pareto set containing 33 solutions was obtained. Figure 8 shows the final Pareto front. The black circle represents the baseline airfoil, the blue triangle represents the optimal airfoil obtained from the single-objective optimization for improving dynamic stall characteristics, and the red squares represent the Pareto front obtained from the multi-objective optimization. It can be noted that the optimal airfoil obtained from the single-objective optimization is included in the end of the Pareto front, indicating that the Pareto optimal solutions from the multi-objective optimization are fully convergent and exhibit diversity. One optimal sample point was selected from the beginning, middle, and end of the Pareto front, resulting in three optimal airfoils: Opt-1, Opt-2, and Opt-3. Figure 9 compares the geometric shapes of the three optimal airfoils. It can be seen that Opt-1 has the largest camber (its geometric shape is quite similar to the optimal airfoil obtained from the single-objective optimization), Opt-3 has the smallest camber, and Opt-2 is intermediate between the two.

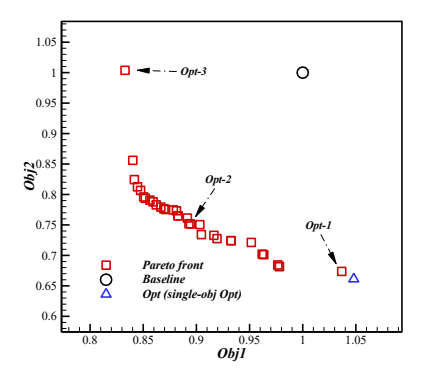


Figure 8 – The approximate Pareto front obtained

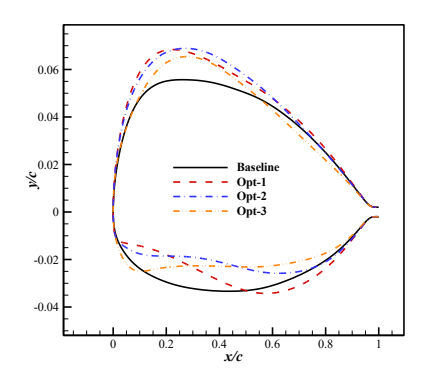


Figure 9 – The geometric shapes of three selected optimal airfoils from Pareto front

According to the distribution of the three selected optimal airfoils on the Pareto front, Opt-1 focuses on dynamic stall characteristics, Opt-3 focuses on static drag characteristics at hovering condition, and Opt-2 strikes a balance between dynamic stall characteristics and static drag characteristics. Figure 10 shows the hysteresis loops of the pitching moment coefficient for the three selected optimal airfoils. The absolute values of their peak pitching moment coefficients and dynamic stall angles of attack are shown in Table 1. The absolute value of the peak pitching moment coefficient for the Opt-1 airfoil is the smallest, reducing by 30.10% compared to the baseline airfoil. The Opt-2 airfoil has the second-best dynamic stall characteristics, with the absolute value of its peak pitching moment coefficient reduced by 19.71% compared to the baseline. The peak pitching moment coefficient of the Opt-3 airfoil is close to that of the baseline airfoil. It can also be seen that the hysteresis loops of the pitching moment coefficient for the Opt-1 and Opt-2 airfoils have only two loops, whereas the Opt-3 and baseline airfoils have three loops. This indicates that the dynamic stall characteristics of the Opt-1 and Opt-2 airfoils are superior to those of the Opt-3 and baseline airfoils, which can also be seen from the hysteresis loops of the lift and drag coefficients in Figure 11.

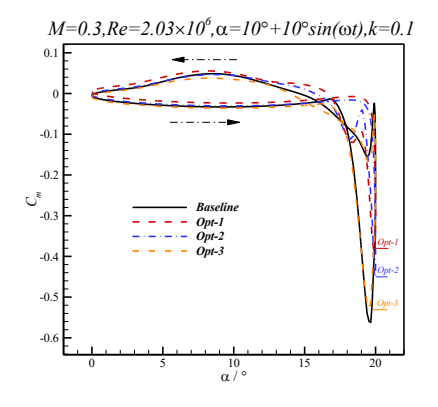
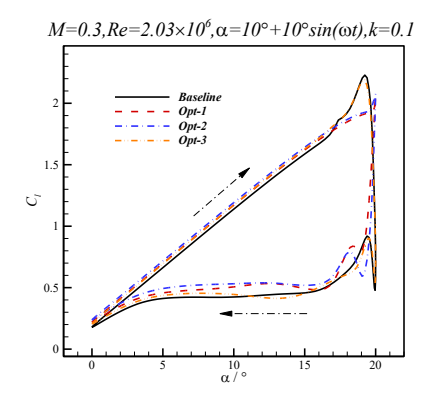
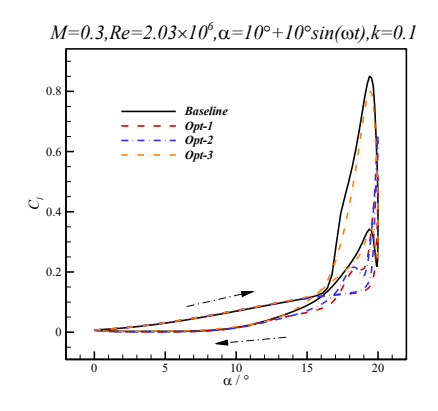


Figure 10 – The hysteresis loops of pitching moment coefficient of three selected optimal airfoils





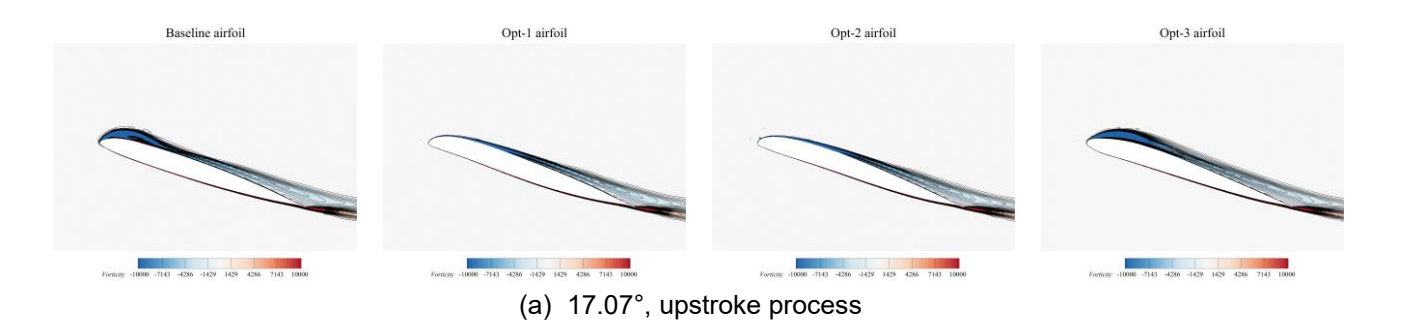
- (a) Hysteresis loop of the lift coefficient
- (b) Hysteresis loop of the drag coefficient

Figure 11 – The hysteresis loops of lift and drag coefficient of the three selected optimal airfoils

Table 1 – The dynamic stall characteristics of the three selected optimal airfoils

	Baseline	Opt-1		Opt-2		Opt-3	
$\mid C_m^i\mid_{\max}$	0.5622	0.3930	-30.10%	0.4514	-19.71%	0.5295	-5.82%
$lpha_{ extit{dynamic stall}}$	19.66°	19.91°	+0.25°	19.99°	+0.33°	19.54°	-0.12°

Figure 12 and Figure 13 show the vorticity contour lines and streamlines comparisons of the baseline airfoil and the three selected optimal airfoils at specific angles of attack. During the upstroke process at an angle of attack of 17.07°, a vortex has already appeared near the leading edge of the baseline and Opt-3 airfoils, while the streamlines over the Opt-1 and Opt-2 airfoils remain attached to their upper surfaces. As the angle of attack increases to 19.66°, the upper surfaces of the baseline and Opt-3 airfoils have completely separated from the leading edge to the trailing edge. Throughout the downstroke process at 19.96° and 7.41°, the vortex on the upper surfaces of the Opt-1 and Opt-2 airfoils remain significantly smaller than those on the baseline and Opt-3 airfoils, effectively suppressing the development of separation vortex. Additionally, among the Opt-1 and Opt-2 airfoils, the vortex suppression effect of the Opt-1 airfoil is slightly better than that of the Opt-2 airfoil.



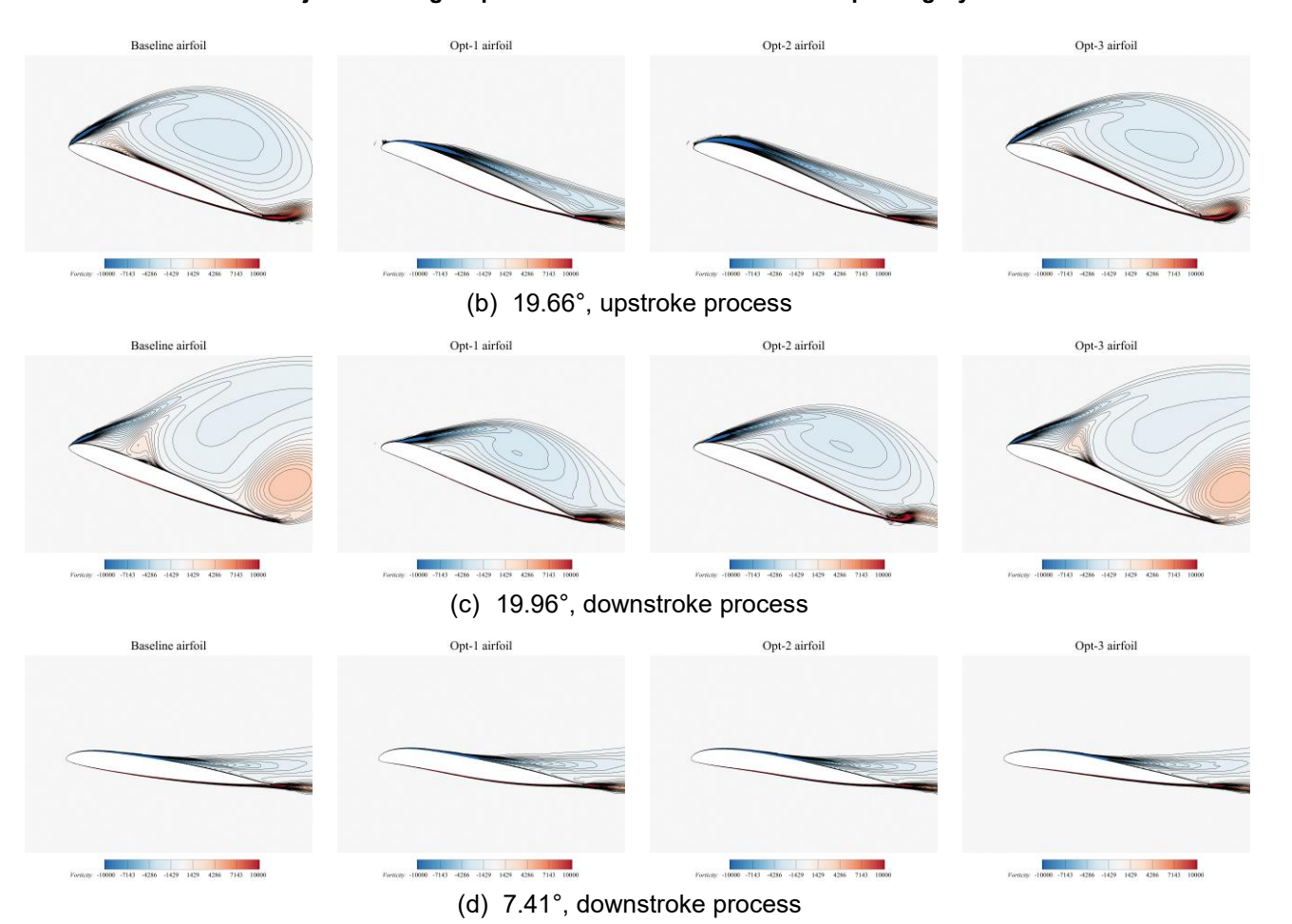
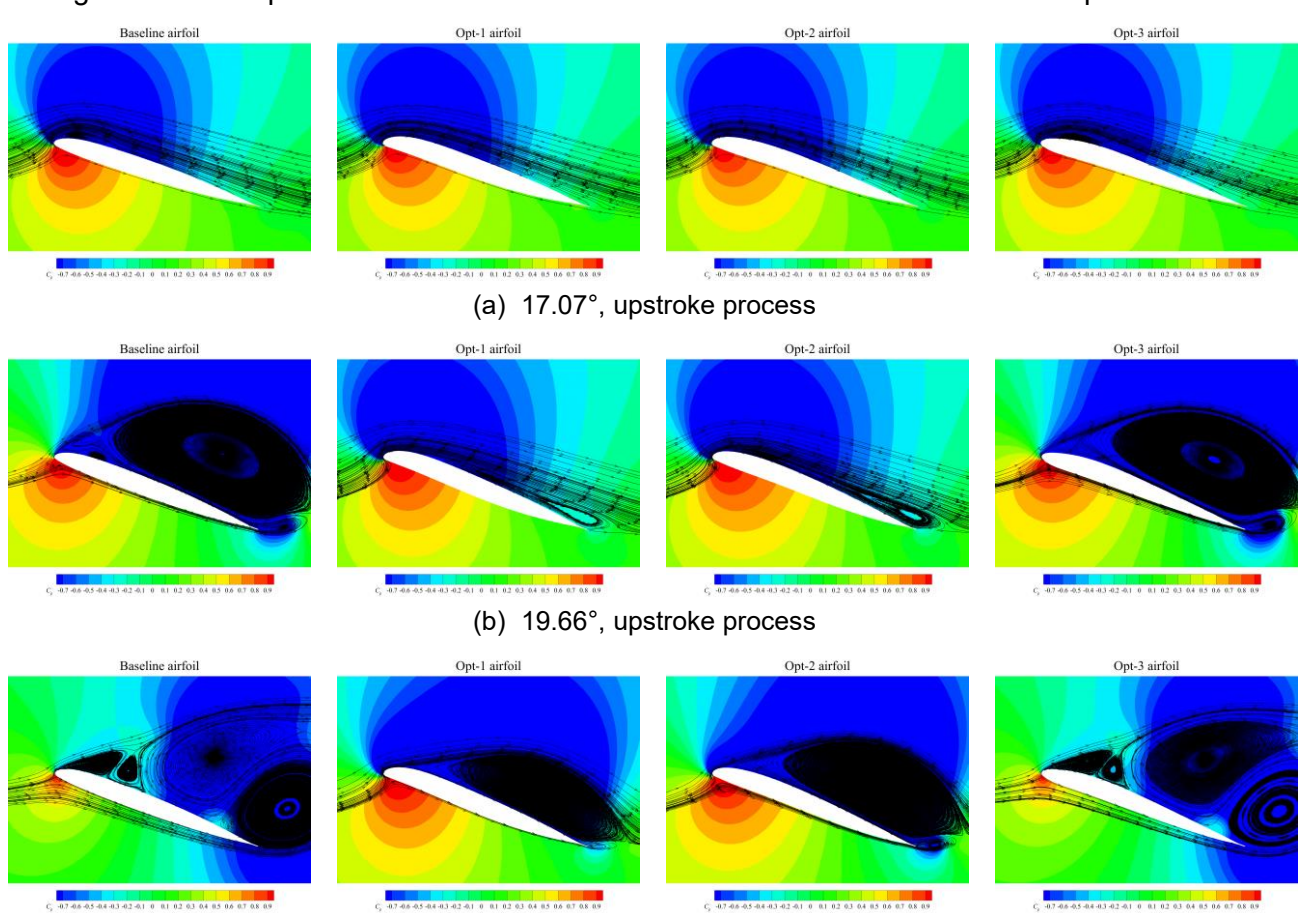


Figure 12 – Comparison of vortex contour lines of baseline and three selected optimal airfoils



(c) 19.96°, downstroke process

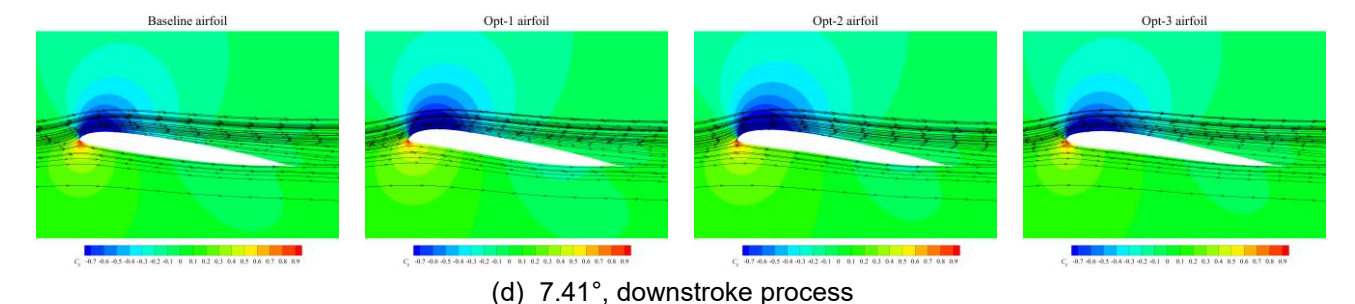


Figure 13 – Comparison of streamlines of baseline and three selected optimal airfoils

As for the static aerodynamic characteristics of the airfoils, as shown in Table 2, the Opt-3 airfoil has the lowest drag coefficient in hovering condition, reducing by 16.57% compared to the baseline. The Opt-2 airfoil follows, while the Opt-1 airfoil performs the worst, with its drag coefficient in hovering even higher than the baseline. Figure 14 shows the pressure distribution of the selected optimal airfoils in hovering condition, where $C_{p,cr}$ represent the critical pressure coefficient. The Opt-1 airfoil has the highest negative peak pressure coefficient on the upper surface and the strongest shock wave, resulting in the highest drag. The Opt-3 airfoil, on the other hand, has the lowest negative peak pressure on the upper surface and even lacks a supersonic region, significantly reducing its drag. The negative peak pressure of the Opt-2 airfoil is between those of the Opt-1 and Opt-3 airfoils. Compared to the baseline, its negative pressure peak is also reduced, leading to a decrease in shock wave drag, and the drag coefficient is reduced by 10.70%. Additionally, as observed from Table 2, the static stall angles of attack of the Opt-1 and Opt-2 airfoils are increased, better than the baseline and Opt-3 airfoils. This indicates that the trends in static stall characteristics and dynamic stall characteristics of the airfoils are generally consistent.

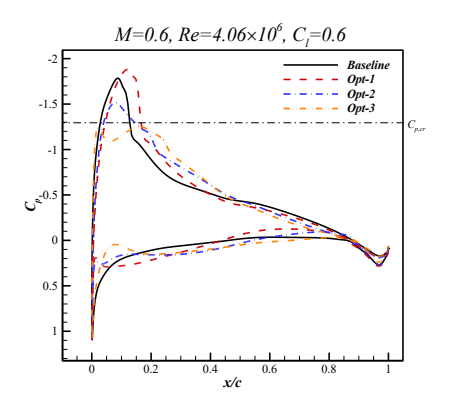


Figure 14 – The pressure coefficient distributions of three selected airfoils at hovering condition

Table 2 – The static aerodynamic characteristics of the three selected optimal airfoils

	Baseline	Opt-1		Opt-2		Opt-3	
C_d at $M = 0.6, C_l = 0.6$	0.00682	0.00707	+3.67%	0.00609	-10.70%	0.00569	-16.57%
$C_{l,\text{max}}$ at $Ma = 0.3$	1.4621	1.5991	+9.37%	1.6084	+10.01%	1.4788	+1.14%
$lpha_{ extit{static stall}}$	13°	14°	+1°	14°	+1°	13°	=

4. Conclusions

In this paper, an efficient design optimization method for rotor airfoils is developed by employing the surrogate-based multi-objective optimization algorithm and an unsteady RANS solver, which is successfully applied to aerodynamic shape optimization for improving dynamic stall characteristics. Additionally, a multi-objective aerodynamic design optimization considering both static aerodynamic characteristics and dynamic stall characteristics of rotor airfoils was conducted. The following conclusions can be drawn:

 The developed method is efficient and robust, demonstrating superior multi-objective optimization design capabilities for rotor airfoils. It can obtain multiple airfoils with different design focuses in one optimization process, allowing designers to choose based on their specific

- The multi-objective design optimization method can be used to enhance the dynamic stall characteristics of the airfoil effectively. The optimized airfoil suppresses the development of dynamic separation vortex, thereby reducing the peak of the pitching moment coefficient, delaying the dynamic stall angle of attack, and significantly improving the dynamic stall characteristics.
- Under the conditions considered in this paper, there is a trade-off between the dynamic stall characteristics and static drag characteristics in hovering condition of rotor airfoils. And the Opt-2 airfoil obtained by the multi-objective design optimization conducted in this paper effectively balances these two aspects. It reduces the peak valve of pitching moment coefficient by 19.71% while also reducing static drag coefficient in hovering condition by 10.70%.

The future work would be focused on considering the drag divergence characteristics at high Mach number of rotor airfoils in a design optimization, which may present a stronger conflict with dynamic stall characteristics at low Mach number. And further developing the multi-objective optimization design method to improve the convergence and distribution of solutions also requires study in future work.

5. Acknowledgments

This work was supported by the National Key Research and Development Program of China under Grant No. 2023YFB3002800 and The Youth Innovation Team of Shaanxi Universities.

6. Contact Author Email Address

Zhong-Hua Han, Professor, hanzh@nwpu.edu.cn, corresponding author.

7. Copyright Statement

The authors confirm that they, and/or their company or organization, hold copyright on all of the original material included in this paper. The authors also confirm that they have obtained permission, from the copyright holder of any third party material included in this paper, to publish it as part of their paper. The authors confirm that they give permission, or have obtained permission from the copyright holder of this paper, for the publication and distribution of this paper as part of the ICAS proceedings or as individual off-prints from the proceedings.

References

- [1] Conlisk A T. MODERN HELICOPTER AERODYNAMICS. Annual Review of Fluid Mechanics. Vol. 29, pp 515–567, 1997.
- [2] Leishman J. Principles of Helicopter Aerodynamics, 2nd edition, Cambridge University Press, 2006.
- [3] Mani K, Lockwood B A, Mavriplis D J. Adjoint-based unsteady airfoil design optimization with application to dynamic stall. AHS Forum. Vol. 68, 2012.
- [4] Wang Q, Zhao Q. Rotor airfoil profile optimization for alleviating dynamic stall characteristics. Aerospace Science and Technology. Vol. 72, pp 502–515, 2018.
- [5] Liu J, Chen R, Lou J, Hu Y, You Y. Deep-learning-based aerodynamic shape optimization of rotor airfoils to suppress dynamic stall. Aerospace Science and Technology. Vol. 133, pp 108089, 2023.
- [6] Raul V, Leifsson L. Surrogate-based aerodynamic shape optimization for delaying airfoil dynamic stall using Kriging regression and infill criteria. Aerospace Science and Technology. Vol. 111, pp 106555, 2021.
- [7] Raul V, Leifsson L. Aerodynamic Shape Optimization for Delaying Dynamic Stall of Airfoils Using Cokriging Regression. AIAA Scitech 2021 Forum. VIRTUAL EVENT, 2021.
- [8] Bu Y-P, Song W-P, Han Z-H, Zhang Y. Efficient aerostructural optimization of helicopter rotors toward aeroacoustic noise reduction using multilevel hierarchical kriging model. Aerospace Science and Technology. Vol. 127, pp 107683, 2022.
- [9] Han S-Q, Song W-P, Han Z-H, Li S-B, Lin Y-F. Hybrid inverse/optimization design method for rigid coaxial rotor airfoils considering reverse flow. Aerospace Science and Technology. Vol. 95, pp 105488, 2019.
- [10]Wang Q, Zhao Q, Wu Q. Aerodynamic shape optimization for alleviating dynamic stall characteristics of helicopter rotor airfoil. Chinese Journal of Aeronautics. Vol. 28, pp 346–356, 2015.
- [11]Kulfan B M. Universal Parametric Geometry Representation Method. Journal of Aircraft. Vol. 45, pp 142–158, 2008.
- [12] Han Z-H, Liu F, Xu C-Z, Zhang K-S, Zhang Q-F. Efficient Multi-Objective Evolutionary Algorithm for Constrained Global Optimization of Expensive Functions. 2019 IEEE Congress on Evolutionary Computation (CEC). pp 2026–2033, 2019.
- [13]Lu Z, Han Z-H, Zhou Z, Song W-P, Zhang Y. Efficient Surrogate-Based Multi-Objective Optimization Algorithm with A New Adaptive Weight Vector Generation. 33rd Congress of the International Council of the Aeronautical Sciences, ICAS 2022, September 4, 2022 - September 9, 2022. Stockholm, Sweden, Vol. 1, pp 538–548, 2022.
- [14]Han Z-H. SurroOpt: a generic surrogate-based optimization code for aerodynamic and multidisciplinary design. Proceedings of ICAS 2016. pp 2016–0281, 2016.
- [15]Krige D G. A statistical approach to some basic mine valuation problems on the Witwatersrand. Journal of the Southern African Institute of Mining and Metallurgy. Vol. 52, pp 119–139, 1951.
- [16] Sacks J, Welch W J, Mitchell T J, Wynn H P. Design and Analysis of Computer Experiments. Statistical Science. Vol. 4, pp 409–423, 1989.
- [17]Han Z, Xu C, Zhang L, Zhang Y, Zhang K, Song W. Efficient aerodynamic shape optimization using variable-fidelity surrogate models and multilevel computational grids. Chinese Journal of Aeronautics. Vol. 33, pp 31–47, 2020.